INTERNATIONAL JOURNAL OF HYDROGEN ENERGY 33 (2008) 878–888

Available at www.sciencedirect.com

journal homepage: www.elsevier.com/locate/ijhydene

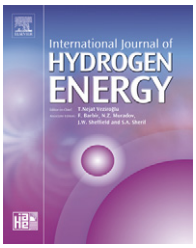

Nozzle injection displacement mixing in a zero boil-off hydrogen storage tank

*Son H. Ho, Muhammad M. Rahman**

Department of Mechanical Engineering, University of South Florida, 4202 E. Fowler Avenue, Tampa FL 33620, USA

ARTICLE INFO

Article history:
Received 10 May 2007
Received in revised form
17 October 2007
Accepted 18 October 2007
Available online 11 December 2007

Keywords:
Liquid hydrogen
Cryogenic storage
Forced convection
Heat transfer

ABSTRACT

This paper presents a steady-state analysis of fluid flow and heat transfer in a zero boil-off cryogenic liquid hydrogen storage tank in microgravity environment. The storage tank is equipped with an assembly of an inlet tube and a nozzle head that contains many nozzles on its front face. Liquid hydrogen is cooled by an external cryocooler, flows along the nozzle head assembly, penetrates into the bulk liquid through the nozzles in order to prevent the boiling off due to heat leak from the surroundings through the tank wall insulation, exits the tank through an annular outlet opening coaxial with the inlet, and then goes back to the external cooling system. Eleven cases for different geometry settings were analyzed. Typical distributions of velocity and temperature are presented. The results show that thermal performance of the system can be improved by increasing the inlet diameter and properly selecting the depth and the span of the nozzle head.

1. Introduction

Hydrogen has been recognized as a powerful and clean fuel for a few decades for space applications [1], and recently for general transportation such as automotives [2]. Hydrogen has been identified to play an important role as an energy source in the future. It has the highest energy content per unit mass of any known fuel. When burned in an engine, hydrogen produces effectively zero emission. When powering a fuel cell, its only waste is water. Hydrogen can be produced from abundant domestic resources including natural gas, coal, biomass, and even water. However, significant technological challenges exist towards reducing its cost and storage volume and assuring its safety. Although hydrogen has many advantages over most conventional fuels, efficient storage of hydrogen is difficult because of its very low density [3]. Cryogenic storage techniques for liquid hydrogen as well as other liquefied gases are of widely increasing interest. Liquid storage of hydrogen has significant advantage over gaseous or chemical storage because of much lower storage volume and ease of regeneration of the fuel with its demand. Since hydrogen has a very low boiling point (20 K at atmospheric pressure, about 1 bar or 0.1 MPa), liquid hydrogen's most challenging aspect in conventional cryogenic storage is the losses due to boil-off under the effect of the heat leakage through the insulation layers of the tank from the surrounding environment. Due to evaporation during boiling-off, vapor pressure increases significantly. In order to control the internal pressure within structural limits of the storage tank, the stored fluid needs to be bled off periodically. The zero boil-off (ZBO) concept has evolved as an innovative means of storage tank pressure control by a synergistic application of passive insulation, active heat removal, and forced mixing within the tank. A cryocooler (with power supply, radiator, and controls) is integrated into a traditional cryogenic storage subsystem to reject the storage system heat leak. Therefore, the hydrogen fuel can be stored for a very long time without any loss.

*Corresponding author. Tel.: +1 813 974 5625; fax: +1 813 974 3539.
E-mail address: rahman@eng.usf.edu (M.M. Rahman).
0360-3199/$ - see front matter © 2007 International Association for Hydrogen Energy. Published by Elsevier Ltd. All rights reserved.
doi:10.1016/j.ijhydene.2007.10.042

Nomenclature

A	radius of cylindrical wall of tank, m
$B-C$	lengths, m
c_p	specific heat of fluid, J/(kg K)
D	inlet diameter, m
D^*	dimensionless inlet diameter, D/A
$F-G$	lengths, m
h	heat transfer coefficient, W/(m^2 K)
H	depth of nozzle head, m
H^*	dimensionless depth of nozzle head, H/A
k	thermal conductivity of fluid, W/(m K)
k_t	turbulent thermal conductivity, W/(m K)
l_c	characteristic length scale of the flow, m
l_m	mixing length, m
l_n	distance from the nearest wall, m
L	span (radius) of nozzle head, m
L^*	dimensionless span of nozzle head, L/A
$M-N$	lengths, m
n	normal direction, m
Nu	Nusselt number, $(2A)h/k$
p	pressure, Pa
$P-Q$	lengths, m
q_w	heat flux at tank wall, W/m^2
r	radial coordinate, m
s	arc length coordinate, m
s^*	dimensionless arc length coordinate, s/A
S	total length of the generatrix of tank wall, m
T	temperature, K
T^*	dimensionless temperature, $(T-T_{in})k/(q_w A)$
T_b	bulk fluid temperature, K
T_{in}	inlet temperature, K
T_w	wall temperature, K
u_r	radial velocity, m/s
u_z	axial velocity, m/s
U	fluid speed, $(u_r^2+u_z^2)^{1/2}$, m/s
U^*	dimensionless speed, U/U_{in}
U_{in}	inlet fluid speed, m/s
V	volume of tank fluid, m^3
z	axial coordinate, m

Greek symbols

δ_i	nominal element size on boundary edges ($i=1,2,3$), m
μ	viscosity of fluid, Pa s
μ_t	Eddy (turbulent) viscosity, Pa s
ρ	density of fluid, kg/m^3
σ_{rr}	radial normal stress, Pa
σ_{rz}	shear stress in $r-z$ plane, Pa
σ_{zz}	axial normal stress, Pa
$\sigma_{\theta\theta}$	Azimuthal normal stress, Pa
Ω	area of the tank wall surface, m^2

In recent years, a number of efforts have been made towards the development of cryogenic storage systems with the ZBO concept. Salerno and Kittel [4] presented the proposed Mars reference mission and the concomitant cryogenic fluid management technology with a combination of both active and passive technologies to satisfy a wide range of requirements. Later, Plachta [5] introduced the ZBO cryogenic storage concept developed at NASA Glenn Research Center. Heat exchanger and integration hardware was bench tested for a large scale demonstration. Hedayat et al. [6,7] presented in details the test set-up and test procedures for the large scale ZBO demonstration. The cryogenic storage system used a cryocooler in addition to traditional passive thermal insulation. The cryocooler was interfaced with the multipurpose hydrogen test bed (MHTB) and spray bar recirculation mixer system in a manner that enabled thermal energy removal at a rate that equals the total tank heat leak. In another report, Hedayat et al. [8] presented analytical models for heat flows through the MHTB tank, cryocooler performance, and spray bar performance.

Kamiya et al. [9,10] presented the development of a large experimental apparatus to measure the thermal conductance of various insulations and used that for the testing of insulation structures. The apparatus could test specimens with dimensions up to 1.2 m diameter and 0.3 m thickness. Hasting et al. [11] presented an overview of NASA's ZBO storage system development, showing that a ZBO system has mass advantage over passive storage. Kittel [12] suggested an alternative approach for the long term storage of cryogenic propellants using a re-liquefier that uses the propellant vapor as the working fluid. Khemis et al. [13] presented an experimental investigation of heat transfer in a cryostat without lateral insulation. Panzarella and Kassemi [14] presented a comprehensive analysis of the transport processes that control the self-pressurization of a cryogenic tank in normal gravity. Mahmoud et al. [15] presented the modeling of the amount of liquid para-hydrogen vaporized during a discharging/charging process in a cryogenic storage system. Reiss [16] presented numerical simulations, using thermal networks, of shield temperature and radiative and conductive heat losses of a super-insulated cryogenic storage tank operating at 77 K. Hofmann [17] presented a theory of boil-off gas-cooled shields for cryogenic storage vessels using an analytical method to determine the effectiveness of intermediate refrigeration. Haberbusch et al. [18] developed a design tool for thermally densified ZBO cryogen storage system for space applications. Wilson et al. [19] did a study with the goal of storing liquid hydrogen in space in a linerless composite tank for a period of 20 years with a 2% boil-off loss.

Venkat and Sherif [20] studied a liquid storage system under normal and reduced-gravity conditions. Mukka and Rahman [21,22] studied the fluid flow and heat transfer in a cryogenic liquid hydrogen storage tank where cool fluid enters the tank at one end, mixes with hot fluid, and exits at the other end. Rahman and Ho [23] studied the fluid flow and heat transfer in a closed ZBO cryogenic storage tank with a heat pipe. Surrounding the heat pipe is an array of many pump-nozzle units that act as an artificial circulatory system.

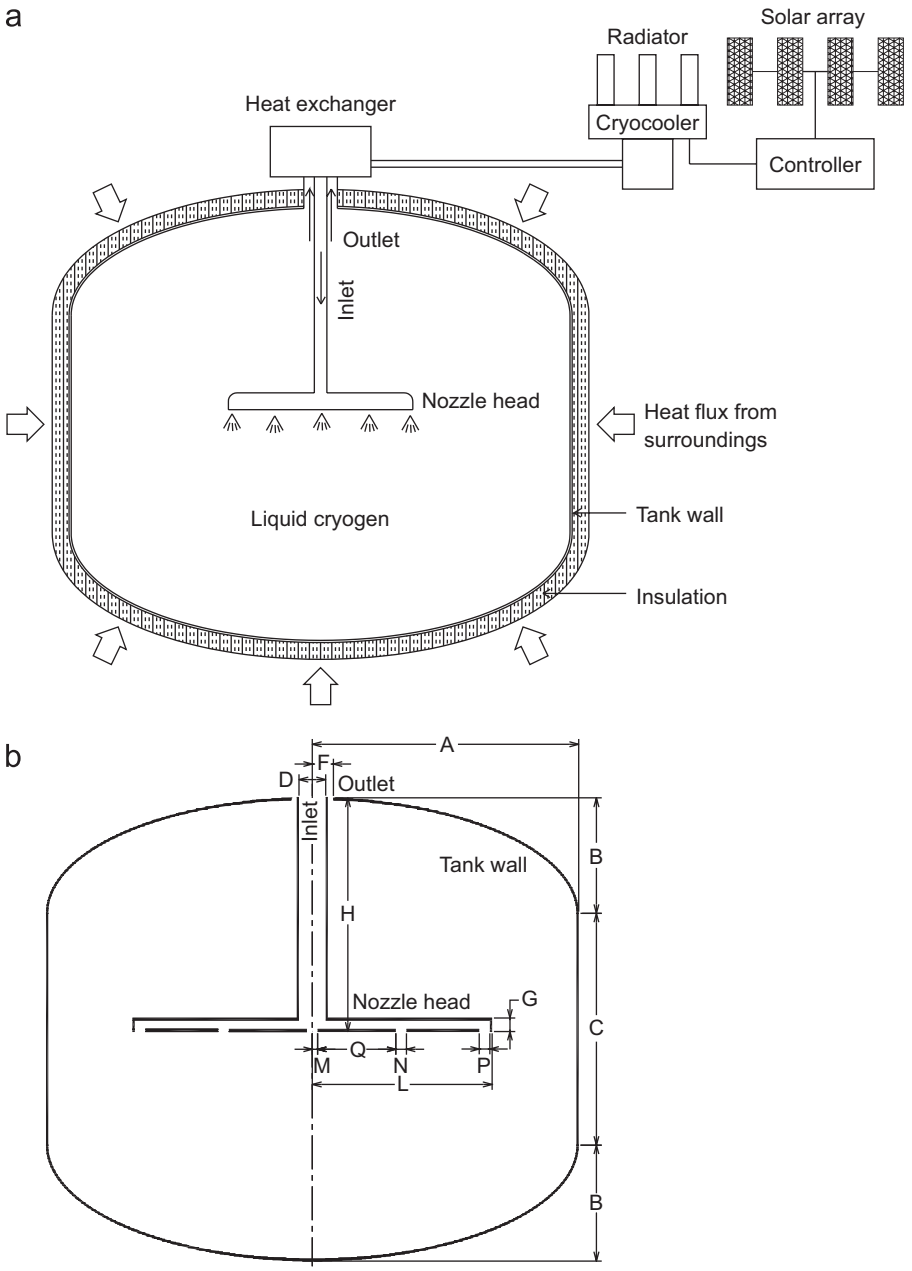

Fig. 1 – Problem description. (a) Schematic diagram of cryogenic storage system; (b) axisymmetric model and essential dimensions.

Later, Ho and Rahman [24] presented a three-dimensional (3-D) analysis for the fluid flow and heat transfer in a similar storage tank with only one pump-nozzle unit. The results showed the complex structures of 3-D distributions of velocity and temperature and the effects of the normal speed at the nozzle face. Recently, Plachta et al. [25] presented passive ZBO storage concepts for both liquid hydrogen and oxygen propellant without cryocoolers. ZBO is achieved by isolating the propellant tank's view to deep space using several shades incorporated to protect the hydrogen tank from the warmer oxygen tank and to protect both tanks from the sun and spacecraft bus.

In this paper, a ZBO cryogenic liquid hydrogen storage system that combines passive insulation and active cooling is proposed. Fig. 1a presents the schematic of a complete system including external cooling system and a cylindrical tank with elliptical top and bottom. The tank wall is made of aluminum and a multi-layered blanket of cryogenic insulation (MLI) has been attached on the top of the aluminum. The tank is filled with liquid hydrogen. An inlet tube is attached to the top shell of the tank at one end and connected to a nozzle head submerged in the liquid at the other end such that the centerline of the whole assembly is coincident with the centerline of the tank. The nozzle head has many nozzles with their centers distributed on concentric circles on its front face. For this study, we consider the nozzle head with three groups of nozzles: one nozzle at the center and two polar arrays of nozzles whose centers are uniformly and

Table 1 – Simulation cases

Simulation #	H (m)	L (m)	D (m)	H^*	L^*	D^*	Notes
1	1.3	1.0	0.15	0.87	0.67	0.10	Base H, L, D values
2	0.8	1.0	0.15	0.53	0.67	0.10	Low H value #1
3	1.1	1.0	0.15	0.73	0.67	0.10	Low H value #2
4	1.5	1.0	0.15	1.00	0.67	0.10	High H value #1
5	1.8	1.0	0.15	1.20	0.67	0.10	High H value #2
6	1.3	0.9	0.15	0.87	0.60	0.10	Low P value
7	1.3	1.1	0.15	0.87	0.73	0.10	High P value #1
8	1.3	1.2	0.15	0.87	0.80	0.10	High P value #2
9	1.3	1.3	0.15	0.87	0.87	0.10	High P value #3
10	1.3	1.0	0.10	0.87	0.67	0.07	Low D value
11	1.3	1.0	0.20	0.87	0.67	0.13	High D value

densely distributed at full span and half span of the nozzle head. The annular outlet opening, also at the top of the tank, is concentric with the inlet opening and its outer radius is calculated such that their cross section areas are the same. Normally, even with the most efficient insulation structure applied, there is always heat leak from the surroundings into the fluid inside the tank. To prevent the heat leak from eventually raising the liquid hydrogen to boiling point, colder liquid hydrogen is pumped through the inlet tube and then injected into the bulk fluid inside the tank through nozzles to displace the heated fluid which exits the tank through the outlet opening on the top shell. The heated fluid then goes into the external cooling system, rejects the heat to cool down and returns to the inlet to complete a working cycle. This study concerns the fluid flow and heat transfer phenomena inside the tank only.

Several parameters can affect the cooling performance of the system. In this study, we consider the effects of the change of the following parameters: the diameter of the inlet tube, the depth of the nozzle head measured from the top of the tank, and the radius of the nozzle head. A parametric analysis is performed to put together an optimum design for the ZBO hydrogen storage system. For doing that, a steady state fluid flow and heat transfer model is set up and solved by using the finite element method. The governing equations for the conservation of mass, momentum, and energy are solved in the fluid domain for the solution of velocity and temperature distributions. Average values and standard deviations of speed and temperature, maximum temperature and wall temperature, and heat transfer coefficient in terms of Nusselt number are computed for assessing the effects of the design parameters on the performance of the system. Standard deviation is used to characterize the non-uniformity of velocity and temperature within the tank which is important in a fluid mixing problem. It is defined as the root mean square (RMS) deviation of temperature values in the entire computational domain from their arithmetic mean (the average temperature). These indicate variation of spatially distributed values, not of values of a random variable (the usual use of standard deviation). The objective in a ZBO cryogenic storage system is to provide the best possible temperature uniformity (lower standard deviation) to eliminate the possibility of local boil-off within the tank. The results will be useful for analysis of the effects of each parameter. The simulation can also be used to optimize the design of a ZBO system for a specific application. It will also give valuable guidelines to designers of ZBO cryogenic storage system in general.

The symmetry of the problem suggests the use of an axisymmetric model instead of costly 3-D model, provided that the nozzles at full span and half span of the nozzle head are distributed dense enough to be approximated as annulus openings. Fig. 1b presents the axisymmetric model with essential dimensions of the tank and the inlet tube-nozzle head assembly. The actual computational domain for the axisymmetric model only occupies the right half of the sketch but the whole axial cross section of the tank is shown for clearer illustration purpose. The cylindrical wall and the ellipsoidal top and bottom are shown as solid curves including a straight line and elliptic arcs. The inlet tube-nozzle head assembly whose axis is coincident with the centerline of the tank and also the z-axis is shown as solid lines with gaps representing three groups of polar distributed nozzle openings.

The essential dimensions are denoted in general form as the capital letters $A-D$, $F-H$, $L-N$, and $P-Q$ in Fig. 1b. The fixed dimensions used in this study are: $A = 1.50\,\text{m}$, $B = 0.65\,\text{m}$, $C = 1.30\,\text{m}$, $G = 0.05\,\text{m}$, $M = 0.01\,\text{m}$, $N = P = 0.02\,\text{m}$. The dimensions D, H, and L are the design parameters under investigation that can take several different values corresponding to eleven simulation cases shown in Table 1. The dimensions F and Q are calculated from the numerical values of the other parameters to satisfy the given requirements (for F, inlet area and outlet area are the same, and for Q, the nozzles in the second group has their centers at half span of the nozzle head) and can be found as

$$F = \frac{D}{\sqrt{2}}, \tag{1}$$

$$Q = \frac{L - (M + N + P)}{2}. \tag{2}$$

Based on the geometric dimensions under study, the volume of the tank, the area of the tank wall surface, and the length of

the generatrix of that surface were, respectively, found as: $V = 15.3\,m^3$, $\Omega = 30.7\,m^2$, and $S = 4.7\,m$.

For better consideration in general context, the geometric design parameters can be presented in dimensionless form by scaling to a characteristic dimension, which is chosen as the radius of the cylindrical wall of the tank A for this study, as

$$D^* = D/A, \tag{3}$$

$$H^* = H/A, \tag{4}$$

$$L^* = L/A. \tag{5}$$

The numerical values of D^*, H^*, and L^* are also given in Table 1.

2. Mathematical model

To describe the fluid flow and heat transfer of liquid hydrogen inside the tank, it is necessary to determine the velocity and temperature distributions in the entire domain by solving the governing equations for the conservation of mass, momentum, and energy. The flow is assumed to be steady, turbulent, and incompressible with constant properties. Reynolds' time average equations are employed to model the turbulent flow. Details on the formulation of the governing equations and Reynolds decomposition approach for turbulence modeling can be found in White [26] and Kays et al. [27]. The equation for the conservation of mass can be written as

$$\frac{1}{r}\frac{\partial}{\partial r}(ru_r) + \frac{\partial u_z}{\partial z} = 0. \tag{6}$$

For a microgravity condition where the gravitational force and the buoyancy effects are negligible, the equation for the conservation of momentum can be written as

$$\rho\left(u_r\frac{\partial u_r}{\partial r} + u_z\frac{\partial u_r}{\partial z}\right) = \frac{1}{r}\frac{\partial}{\partial r}(r\sigma_{rr}) - \frac{\sigma_{\theta\theta}}{r} + \frac{\partial \sigma_{rz}}{\partial z}, \tag{7}$$

$$\rho\left(u_r\frac{\partial u_z}{\partial r} + u_z\frac{\partial u_z}{\partial z}\right) = \frac{1}{r}\frac{\partial}{\partial r}(r\sigma_{rz}) + \frac{\partial \sigma_{zz}}{\partial z}, \tag{8}$$

where

$$\sigma_{rr} = -p + 2(\mu + \mu_t)\frac{\partial u_r}{\partial r}, \tag{9}$$

$$\sigma_{\theta\theta} = -p + 2(\mu + \mu_t)\frac{u_r}{r}, \tag{10}$$

$$\sigma_{rz} = (\mu + \mu_t)\left(\frac{\partial u_r}{\partial z} + \frac{\partial u_z}{\partial r}\right), \tag{11}$$

$$\sigma_{zz} = -p + 2(\mu + \mu_t)\frac{\partial u_z}{\partial z}. \tag{12}$$

For turbulence modeling, the effective viscosity is defined as the sum of the dynamic viscosity μ (physical property) and eddy viscosity μ_t (representing effects of turbulent flow) in Eqs. (9)–(12). To estimate the eddy viscosity, the mixing length model is used. This model is a simple yet effective turbulence model involving a single unknown parameter called mixing length or the mean free path for the mixing of turbulent fluid flow. The mixing length model works well for relatively simple flows such as wall boundary-layer, jet, and wake flows without requiring any additional governing equations. For the problem at hand, this turbulence model can be employed if we consider that the rather complex flow in the computational domain has several regions of simple turbulent flows (wall boundary-layer and jet). If the regions of simple turbulent flows are separated far enough, the transport and history effects of turbulence are insignificant. Details on this turbulence model can be found in Kays et al. [27] and Rodi [28]. The eddy viscosity can be written using tensor notation as

$$\mu_t = \rho l_m^2\sqrt{\left(\frac{\partial u_i}{\partial x_j} + \frac{\partial u_j}{\partial x_i}\right)\frac{\partial u_i}{\partial x_j}}, \tag{13}$$

where

$$l_m = \min(0.41 l_n, 0.09 l_c). \tag{14}$$

l_n is the distance from the nearest wall to a point. l_c is a characteristic length scale for the flow, taken as the largest value of l_n in the computational domain.

Assuming that there is no heat generation and viscous dissipation and pressure work are negligible, the equation for the conservation of energy can be written as

$$\rho c_p\left(u_r\frac{\partial T}{\partial r} + u_z\frac{\partial T}{\partial z}\right) = \frac{1}{r}\frac{\partial}{\partial r}\left[(k + k_t)r\frac{\partial T}{\partial r}\right] + \frac{\partial}{\partial z}\left[(k + k_t)\frac{\partial T}{\partial z}\right]. \tag{15}$$

Similar treatment as that for viscosity is also applied for the effective thermal conductivity with the additional turbulent thermal conductivity k_t in Eq. (15). The turbulent thermal conductivity can be expressed as

$$k_t = \frac{c_p\mu_t}{0.85}. \tag{16}$$

To completely define the problem, appropriate boundary conditions are applied on every boundary segment of the computational domain. These can be described as follows:

On inlet opening:

$$u_r = 0, \quad u_z = U_{in}, \quad T = T_{in}. \tag{17}$$

On centerline:

$$u_r = 0, \quad \frac{\partial u_z}{\partial r} = 0, \quad \frac{\partial T}{\partial r} = 0. \tag{18}$$

On tank wall:

$$u_r = u_z = 0, \quad k\frac{\partial T}{\partial n} = q_w. \tag{19}$$

On inlet tube and nozzle head wall:

$$u_r = u_z = 0, \quad \frac{\partial T}{\partial n} = 0. \tag{20}$$

3. Numerical solution

Governing equations and boundary conditions, Eqs. (6)–(20), are simultaneously solved using the finite element method. The computational domain is discretized into a mesh of finite elements. In each element, radial and axial velocity components, pressure, and temperature are approximated by using the Galerkin procedure [29], which leads to a set of nonlinear algebraic equations that defines the discretized continuum.

The fully coupled successive substitution algorithm is employed to solve the system of nonlinear equations. Two convergence criteria are used: the relative error criterion that checks if the relative error at an iteration is less than a preset tolerance, and the residual criterion that checks whether the ratio of the residual vector at an iteration to a reference residual vector is less than another preset tolerance. The iterative procedure is considered converged when both criteria are satisfied. The tolerances for the present simulations are 0.0001 for both relative error and residual.

For all simulations, meshes of four-node quadrilateral elements were used. The size of the mesh was controlled by adjusting the element size on the boundary edges of solid fluid interfaces. Due to the complexity of the geometry, three nominal element sizes were used for three groups of boundary edge segments. The first one δ_1 is for large size edge segments such as those that form the tank wall. The second one δ_2 is for medium size edge segments such as inlet and outlet openings. The third one δ_3 is for the small size edge segments such as nozzle openings and also for general use where finer mesh was required. Each boundary edge segment was meshed by using double-sided grading meshing scheme such that two elements at both ends have the size of δ_3 and the elements inside have increasing sizes toward the center of the segment with a single growth ratio dependent on the length of the edge segment and its nominal size δ_i. Similarly, the height of the element layers from the solid-fluid interface increased inward the fluid body by a factor of 1.25 starting with δ_3 at the interface. These layers of structured mesh of smaller size elements cover the region with high rates of momentum and heat transfer. Beyond these layers, the rest of the computational domain was paved with an unstructured mesh of quadrilateral elements.

The distribution of element size in the computational domain was determined from a mesh independence study by systematically changing the mesh density in all space directions both globally and locally to obtain a mesh that can give a numerical solution of acceptable accuracy. The final set of mesh sizes have $\delta_1 = 0.012\,\text{m}$, $\delta_2 = 0.010\,\text{m}$, and $\delta_3 = 0.004\,\text{m}$. For a mesh independence study, different cases of mesh size were considered. Taking the final set of mesh sizes as the reference, simulations for the base case of geometry settings were performed using 16, 12, 8, 4, 3, 2, 1.5, 1 (reference), and 0.75 times the reference mesh size or 378, 580, 935, 2685, 4302, 8905, 15 488, 33 671 (reference), and 57 019 quadrilateral elements. Fig. 2 shows how the fluid temperature at representative locations in the tank becomes independent of the mesh size as the number of elements increases (the element size decreases). Fig. 2a presents the radial distribution of temperature on a section perpendicular to the centerline of the tank and at a distance of 0.1 m from the nozzle head ($z = 1.4\,\text{m}$). Fig. 2b presents the values of average temperature and temperatures at three locations as functions of the number of elements. Fig. 2a and b demonstrate that as the number of elements increases over 20 000, a mesh independence of the numerical solution is achieved. The mesh with 33 671 elements was found quite adequate for accurate numerical prediction. Therefore, the reference set of mesh sizes was used for generating the meshes for all simulation cases presented in this paper. Due to different

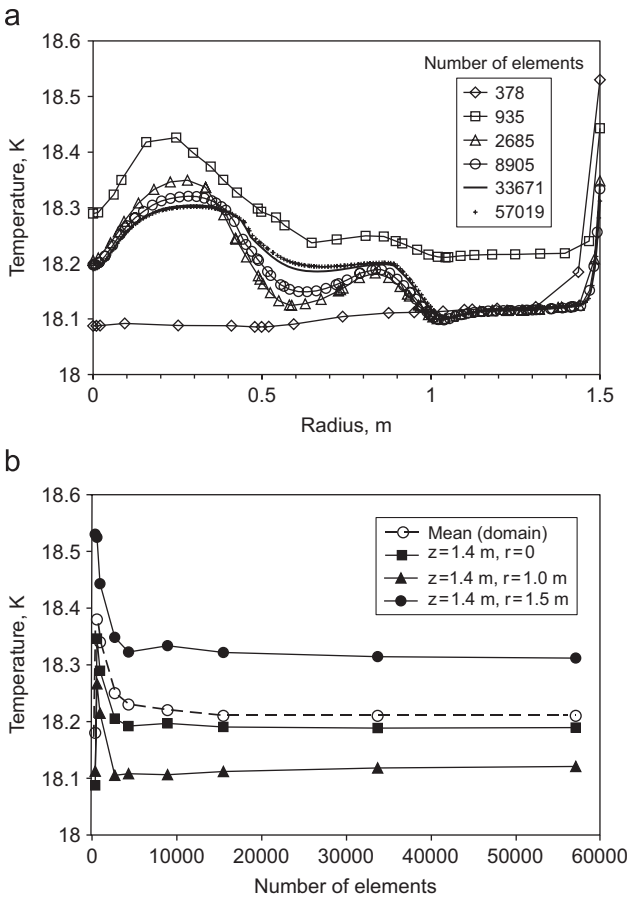

Fig. 2 – Grid independence. (a) Temperature solution on section $z = 1.4\,\text{m}$; (b) temperature solution as function of number of elements.

geometry settings, the number of quadrilateral elements in these meshes slightly varies from case to case within the range 33 000–34 000.

The input needed is the numerical values of physical properties and boundary conditions. Relevant properties of liquid hydrogen are taken as constants at a reference temperature of 20 K as $\rho = 71.1\,\text{kg/m}^3$, $\mu = 13.6 \times 10^{-6}\,\text{Pa s}$, $c_p = 9.53 \times 10^3\,\text{J/(kg K)}$, $k = 0.0984\,\text{W/(m K)}$. Prescribed values for boundary conditions include: inlet velocity $U_{\text{in}} = 0.01\,\text{m/s}$, inlet temperature $T_{\text{in}} = 18\,\text{K}$, and heat flux on the tank wall $q_{\text{w}} = 1\,\text{W/m}^2$.

The numerical solution obtained by solving Eqs. (6)–(20) gives four primary parameters: two velocity components, pressure, and temperature distributed over the entire computational domain. Due to lack of any experimental data for the problem considered here, a direct validation of results was not possible. In addition to a very careful grid independence study as mentioned above, all runs were checked for energy balance by comparing the integrated total heat leak into the tank with heat carried away by convection determined from average inlet and outlet temperature of the fluid. This energy balance checked within 0.2–0.9%. These may be adequate to prove that computed results are mesh independent and accurate.

4. Results and discussion

Fig. 3 shows the distributions of fluid velocity and temperature for the base case (simulation 1). In Fig. 3a, the color of the filled background represents speed (the magnitude of velocity) and the streamlines shows the directions of the fluid flow. In Fig. 3b, the temperature distribution is shown by a filled plot with the color representing the value of temperature. The cold fluid enters the inlet opening at full speed U_{in} and flows along the inlet tube as a typical flow in circular pipe to the nozzle head and the spreads radially inside the nozzle head before injecting into then bulk fluid. Temperature inside the inlet tube and the nozzle head does not change much thus quite uniform and as low as the inlet temperature. Once the flow reaches the front face of the nozzle head, it splits into three groups of flow (numbered 1, 2, and 3 in Fig. 3a) corresponding to three groups of nozzle openings on the nozzle head. The first group goes straight ahead through the center nozzle and directly injects into the bulk fluid at a speed as high as that at the inlet opening, creates a disturbance in a local region along the centerline and gets retarded shortly by the massive stagnant bulk fluid at the bottom of the tank. This flow gives the bulk fluid a small region of low temperature localized along the centerline right outside the nozzle. As the rest of the fluid spreads in radial direction inside the nozzle head, the flow cross section area increases thus the fluid velocity decreases and the flow loses momentum. The flow tends to remain on its radial direction and travel the full span of the nozzle head rather than to change direction to exit at half span. Therefore the second group of flow corresponding to the second nozzle group is quite weak and only can create small disturbances locally. The third nozzle group at full span of the nozzle head is where the supply cold fluid injects into the bulk fluid more strongly and shows significant effects on cooling. Also drawn by the pressure gradient toward the outlet opening, the flow exits the nozzle head at a direction that bends toward the wall of the tank. It reaches the wall and then moves upward while sweeping along the wall toward the outlet opening at quite high speed due to the influence of the low pressure there. Under the effect of this flow, a strong circulation is formed in the region above the nozzle head (marked as C_1 in Fig. 3a). This circulation creates a well mixed thus low temperature region there. Since this flow cannot reach the top shell of the tank, a region of stagnant fluid (marked as S_1 in Fig. 3b) exists there. It can be observed in Fig. 3b that this region has higher temperature and that temperature decreases from the wall inward in isothermal layers that shows the heat conduction pattern. As the third flow injects into the bulk fluid, it also affects the region under the nozzle head by combining with the second flow to form a circulation there (marked as C_2 in Fig. 3a) resulting in another well mixed region of low temperature but not as low as the one in the region above the nozzle head. The fluid between this region and the low temperature region created by the first flow is barely moved and results in higher temperature (marked as S_2 in Fig. 3b). The spot of maximum temperature can be resided in one of these two stagnant regions and right at the tank wall.

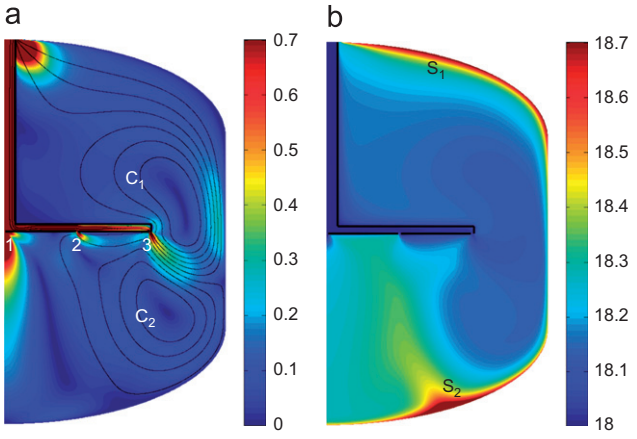

Fig. 3 – Distributions of velocity and temperature, simulation 1 (base case). (a) Streamlines and speed, mm/s; (b) temperature, K.

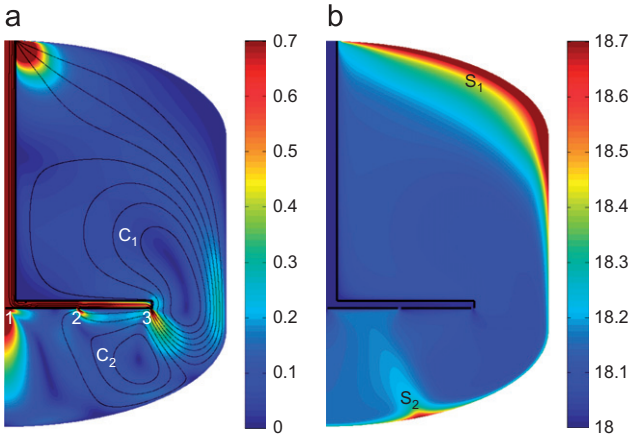

Fig. 4 – Distributions of velocity and temperature, simulation 5 ($H^* = 1.2$). (a) Streamlines and speed mm/s; Temperature, K.

The patterns of fluid flow and temperature distributions shown above suggests that if the nozzle head is placed deep down toward the bottom of the tank, it may extend the well mixed region above the nozzle head as well as reduce the stagnant region under it thus improve the cooling performance of the system. Fig. 4 shows the velocity field and temperature distribution for simulation 5 which has the largest value of the nozzle head depth H among the simulations. It can be observed that the patterns of both velocity and temperature distributions are similar to those of the base case. The well mixed-low temperature region above the nozzle head extended as expected. The region under the nozzle head has a lower and more uniform temperature compared to that of the base case especially in the stagnant-higher temperature region at the bottom of the tank (marked as S_2 in Fig. 4b). However, since the nozzle head is put that far away from the top, the fluid has to travel a longer distance to reach the top of the tank toward the outlet. Therefore, it cannot reach as closely to the top shell of the tank wall as in the base case to transport the heat away and reduce the temperature there. As a result, the region of stagnant fluid of

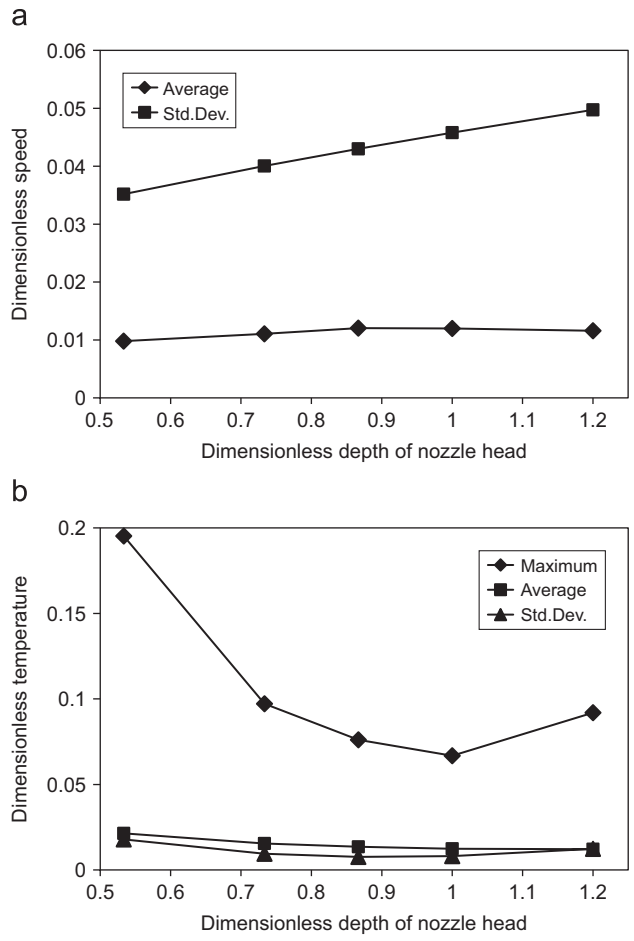

Fig. 5 – Effect of depth of nozzle head on distributions of (a) speed and (b) temperature.

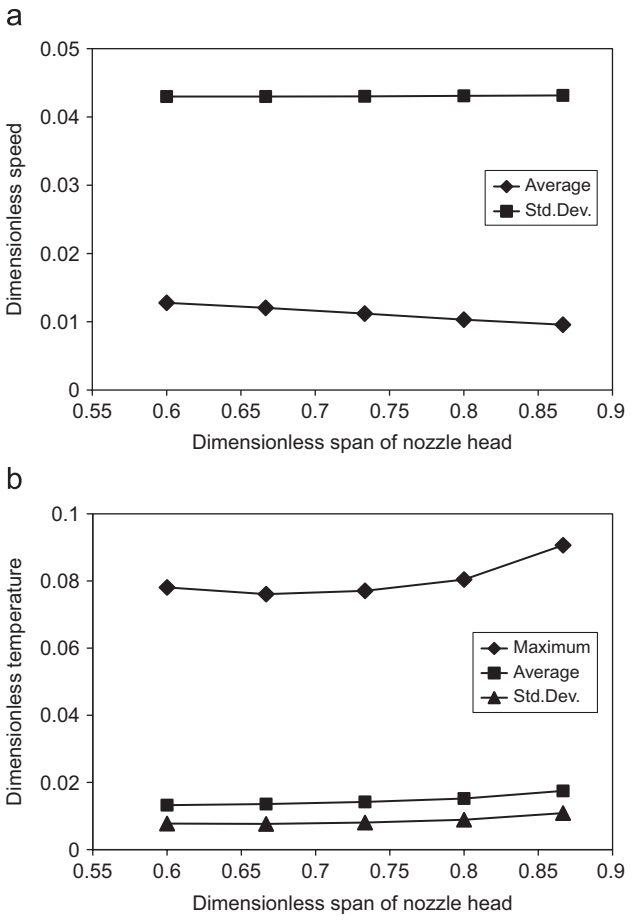

Fig. 6 – Effect of span of nozzle head on distributions of (a) speed and (b) temperature.

high temperature there (marked as S_1 in Fig. 4b) expands much larger. That means there will be more chances for a higher maximum temperature spot to exist in that region.

The effects of a design parameter on the distributions of speed and temperature can be studied quantitatively by considering the average speed and the standard deviation of speed as well as the maximum and average temperatures and the standard deviation of temperature. At a point in the computational domain, fluid speed can be found by

$$U = \sqrt{u_r^2 + u_z^2}. \tag{21}$$

Fluid speed and temperature are presented in dimensionless form as

$$U^* = \frac{U}{U_{in}}. \tag{22}$$

$$T^* = \frac{(T - T_{in})k}{q_w A}. \tag{23}$$

Fig. 5 presents the effects of the depth of the nozzle head on the distributions of speed and temperature. The results are from simulations 1–5. These five cases adopt the same set of values for all geometric parameters except that each of them has a different value of H. The depth of the nozzle head H is measured from the top of the tank to the front face of the nozzle head and presented in its dimensionless form H^*. In Fig. 5a, the dimensionless speed of the fluid show no significant changes around 0.01 for any H^* but the dimensionless standard deviation increases linearly from 0.035 to 0.050 as H^* increases. This suggests that the depth of the nozzle head has no significant effect on the average speed field but increase its non-uniformity. In Fig. 5b, as H^* increases from 0.53 to 1.20, the dimensionless maximum temperature decreases from 0.2, reaches it minimal value of 0.07 at $H^* = 1$, then increases again to 0.09 at $H^* = 1.20$. The dimensionless standard deviation varies from 0.02 to 0.01 in a similar trend. On the other hand, the dimensionless mean temperature gradually decreases from 0.02 to 0.01 as H^* increases from 0.53 to 1.20. These results confirm the previous observations that as the nozzle head is located closer to the bottom of the tank, lower average temperature can be achieved but maximum temperature may become higher if H^* increases further from an optimum range of $H^* = 0.9-1.0$. In actual dimensions, this range is corresponding to about the middle of the height of the tank slightly shifted toward the bottom.

Fig. 6 presents the results from simulations 1 and 6–9 on the effects of the span (radius) of the nozzle head L represented by its dimensionless form L^*. The increase of L is in fact the increase of nozzle openings area for the second and third groups of nozzles. In Fig. 6a, it is observed that as L^* increases

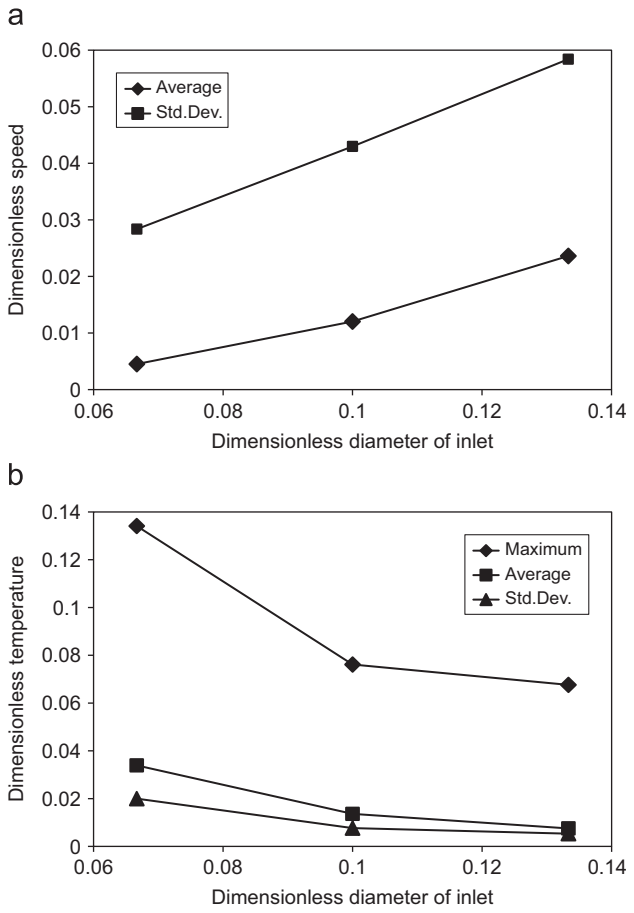

Fig. 7 – Effect of inlet diameter on distributions of (a) speed and (b) temperature.

from 0.60 to 0.87, the dimensionless average speed decreases linearly and very slightly from 0.013 to 0.010 while the dimensionless standard deviation remains at a value of 0.043. This suggests that the span of the nozzle head has no significant effect on speed distribution. Fig. 6b shows that all the parameters of temperature distribution increase as L^* increases from 0.60 to 0.87, dimensionless maximum temperature from 0.08 to 0.09, dimensionless average temperature from 0.01 to 0.02, and dimensionless standard deviation from 0.008 to 0.011. A good value of L^* can be selected around the base value $L^* = 0.67$ in the range 0.6–0.75 without any significant effects on average and maximum temperatures and standard deviation.

Fig. 7 presents the effects of the inlet diameter D to the distributions of speed and temperature from the results of simulations 1 and 10–11. These three simulations have the same set of geometric parameters except that each simulation has a different value of D. It can be observed in Fig. 7a that both dimensionless average speed and standard deviation increase in a linear fashion as the dimensionless diameter of inlet D^* increases from 0.07 to 0.13, in the ranges 0.005–0.024 and 0.028–0.058, respectively. This suggests that increasing inlet diameter results in higher fluid speed overall—which is well expected since the change of the inlet diameter is directly proportional to the change of supply flow rate while the inlet velocity remains the same—and higher non-uniformity in the flow speed field. Fig. 7b shows that both the dimensionless maximum and mean temperatures decrease from 0.13 to 0.07 and from 0.03 to 0.01 K, respectively, as D^* increases from 0.07 to 0.13. This is also well expected since higher inlet diameter with the same inlet velocity results in higher flow rate of supply cold fluid, and therefore lower maximum and average temperatures within the tank. However, as D^* increases, the slope of the temperature curve reduces significantly, implying that the inlet diameter should be designed at a proper value such that the positive effects it brings should over-compensate the energy used for pumping fluid at higher flow rate. For the same range of D^*, the dimensionless standard deviation of temperature also decreases from 0.02 to 0.005, which shows that mixing effectiveness (more uniform temperature distribution) can also be improved with higher flow rate.

The thermal performance of the system can also be assessed by looking into the distribution of heat transfer coefficient defined as

$$h = \frac{q_w}{T_w - T_b}, \tag{24}$$

where the bulk fluid temperature or the average fluid temperature in the tank can be defined as

$$T_b = \frac{1}{V}\int_{(V)} T\,dV. \tag{25}$$

Wall temperature extracted from the temperature solution for each simulation varies along the generatrix of the surface of revolution that forms the tank wall and can be presented as a function of the arc length coordinate measured from the center of the bottom of the tank. The arc length coordinate is scaled in the dimensionless form as

$$s^* = s/A. \tag{26}$$

The heat transfer coefficient can be expressed in term of the dimensionless Nusselt number ($Nu = (2A)h/k$) as

$$Nu = \frac{(2A)q_w}{k(T_w - T_b)}. \tag{27}$$

The average Nusselt number can be computed by using numerical integration as

$$\overline{Nu} = \frac{1}{\Omega}\int_{(\Omega)} Nu\,d\Omega. \tag{28}$$

Fig. 8 shows the dimensionless wall temperature and Nusselt number with selected cases of geometry settings with base, low, and high values for each geometric parameter. The base case has $H^* = 0.87$, $P^* = 0.67$, and $D^* = 0.10$ ($H = 1.3$ m, and $P = 1.0$ m, $G = 0.15$ m). The legends for other cases only show the parameter that is different from the base case. Since the highest temperature should be located at the wall where the heat flux is applied, the maximum wall temperature is also the maximum temperature in the entire fluid body. In Fig. 8a, it can be observed that for most cases there are two peaks or raising regions on the graph representing two stagnant regions of high temperature. The case of $H^* = 0.53$ (low H) have only one outstanding peak at the bottom of the tank. This is the case where the nozzle head is very close to the top and therefore the stagnant region at the top is eliminated but the stagnant region at the bottom is expanded to a wide region with highest maximum temperature

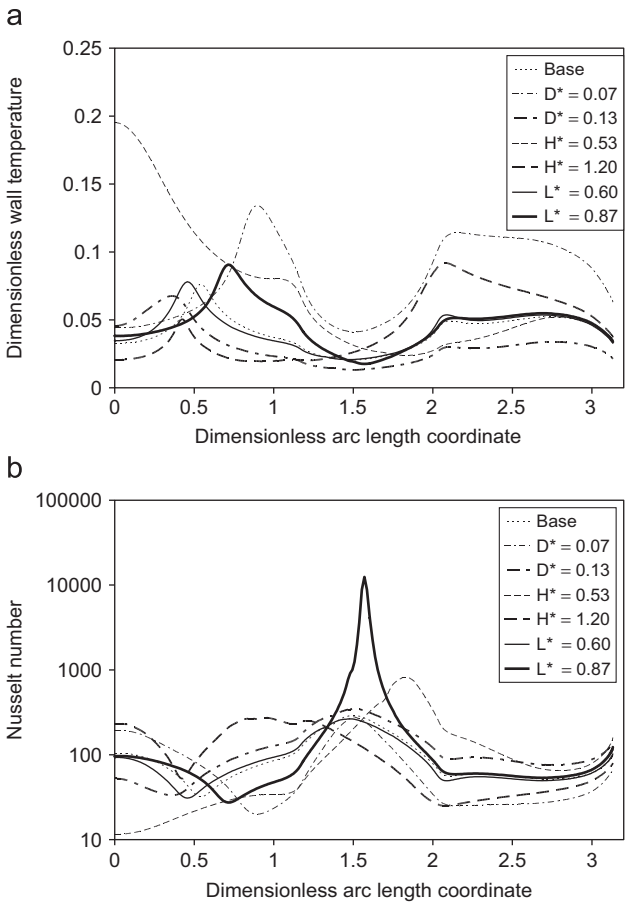

Fig. 8 – Effect of geometry settings on (a) wall temperature and (b) local Nusselt number.

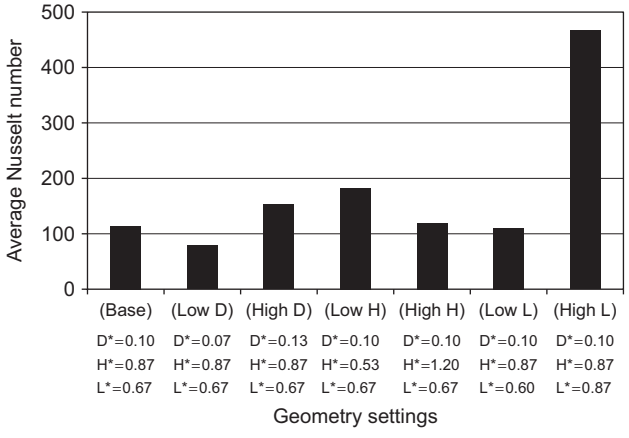

Fig. 9 – Average Nusselt number as function of geometry setting.

compared to that of other cases. The base case as well as most of the other cases has the notably higher first peak (stagnant region at the bottom) and the second peak (stagnant region at the top) leveled out except for the case $H^* = 1.2$ (high H) where both peaks are shown and the peak at the top is higher than the peak at the bottom. This means that the maximum temperature spot is resided in the stagnant region at the top for the case of high H and in the stagnant region at the bottom for the rest. As D^* decreases, the maximum temperature spot increases in magnitude as expected and moves far away from the center of the bottom. Lowest wall temperature found for the case $D^* = 0.13$ (high D) is also well expected.

Fig. 8b shows Nusselt numbers for the same set of cases of geometry settings as functions of dimensionless arc length coordinate. Higher Nusselt number means more efficient convective heat transfer. Since Nusselt number is inversely proportional to $(T_w - T_b)$ whereas dimensionless temperature is proportional to $(T_w - T_{in})$, the profile of the former is similar to that of the latter being flipped over. For all cases, Nusselt number ranges from 12 to 12444 with the maximum value belongs to the case of $L^* = 0.87$ at the middle of the tank wall.

Fig. 9 presents the average Nusselt numbers as functions of geometry settings. The data were extracted from the same representative set of simulations described above. In general, the average Nusselt number ranges from 78 to 467. Lower and higher D gives lower and higher Nusselt number, respectively. This means that as the inlet diameter increases thus flow rate increases, the average condition of convective heat transfer in the system is improved. If the flow rate is kept unchanged, altering the depth of the nozzle head H from the base value, either lower or higher, can be employed to enhance average convective heat transfer. However, this approach should be used with caution since it may increase the maximum temperature as discussed previously (Fig. 5b). Increasing the span of the nozzle head L yields a significant increase on the average Nusselt number but it also results in higher maximum temperature as mentioned above (Fig. 6b).

5. Conclusions

The numerical simulations give better understanding of the fluid flow and heat transfer phenomena needed for the design of a cryogenic storage tank for liquid hydrogen. For this design with the nozzle head, the cold fluid discharged through the nozzle penetrates into the bulk fluid medium inside the tank as a submerged jet and mixes with the fluid as it loses momentum. It is found that higher temperature is encountered near the tank wall at two locations on the top and bottom. The nozzle head is best located in the middle part of the tank since this yields lower maximum temperature. As inlet diameter increases while inlet velocity is unchanged, supply flow rate increases and results in lower maximum and mean temperatures. However, higher flow rate requires higher energy consumption for running the pump and the cryocooler. Therefore, this parameter needs to be designed in interaction with others to obtain optimum efficiency for the whole system. The increase of the span of the nozzle head that implies the increase of total nozzle openings area results in a slightly rise of both maximum and mean temperatures. It is best to keep that parameter in the range of 0.60–0.75 the radius of the tank. These guidelines are useful in designing and optimizing ZBO cryogenic storage systems.

Acknowledgments

The financial support for this research was received from National Aeronautics and Space Administration (NASA) under Contract number NAG3-2751. The information provided by David Plachta at NASA-Glenn is gratefully acknowledged.

REFERENCES

[1] Dawson VP, Bowles MD. Taming liquid hydrogen: the Centaur upper stage rocket 1958–2002. Washington, DC: NASA; 2004.
[2] Uhrig RE. Heading toward hydrogen. Energy 2004;29(2): 17–21.
[3] Colozza AJ. Hydrogen storage for aircraft applications overview. NASA report no. NASA/CR-2002-211867. Washington, DC: NASA; 2002.
[4] Salerno LJ, Kittel P. Cryogenics and the human exploration of Mars. Cryogenics 1999;39:381–8.
[5] Plachta DW. Zero-boiloff cryogenic storage cryocooler integration test. Technical report, NASA; 2001.
[6] Hedayat A, Hastings LJ, Bryant C, Plachta DW. Cryogenic propellant long-term storage with zero boil-off. Technical report NAS8-00187, NASA; 2001.
[7] Hedayat A, Hastings LJ, Bryant C, Plachta DW. Large scale demonstration of liquid hydrogen storage with zero boiloff. In: Advances in cryogenic engineering: proceedings of the cryogenic engineering conference (CEC), AIP conference proceedings, vol. 613, 2002. p. 1276–83.
[8] Hedayat A, Hastings LJ, Sims J, Plachta DW. Cryogenic propellant long-term storage with zero boil-off. Technical report NAS8-40836, NASA; 2001.
[9] Kamiya S, Onishi K, Kawagoe E, Nishigaki K. A large experimental apparatus for measuring thermal conductance of LH2 storage tank insulations. Cryogenics 2000;40:35–44.
[10] Kamiya S, Onishi K, Kawagoe E, Nishigaki K. Thermal test of the insulation structure for LH2 tank by using the large experimental apparatus. Cryogenics 2001;41:737–48.
[11] Hastings LJ, Plachta DW, Salerno L, Kittel P. An overview of NASA efforts on zero boiloff storage of cryogenic propellants. Cryogenics 2002;41:833–9.
[12] Kittel P. Propellant preservation using re-liquefiers. Cryogenics 2002;41:841–4.
[13] Khemis O, Boumaza M, Ait Ali M, Francois MX. Experimental analysis of heat transfers in a cryogenic tank without lateral insulation. Appl Thermal Eng 2003;23(16):2107–17.
[14] Panzarella CH, Kassemi M. On the validity of purely thermodynamic descriptions of two-phase cryogenic fluid storage. J Fluid Mech 2003;484:41–68.
[15] Mahmoud AM, Lear WE, Sherif SA. Transient analysis of pressure-induced transfer of cryogenic hydrogen in storage systems. In: Proceedings of the 42nd AIAA aerospace sciences meeting and exhibit, 2004. p. 1091–102.
[16] Reiss H. A coupled numerical analysis of shield temperatures, heat losses and residual gas pressures in an evacuated super-insulation using thermal and fluid networks—part I: stationary conditions. Cryogenics 2004;44(4):259–71.
[17] Hofmann A. Theory of boil-off gas cooled shields for cryogenic storage vessels. Cryogenics 2004;44:159–65.
[18] Haberbusch MS, Stochl RJ, Culler AJ. Thermally optimized zero boil-off densified cryogen storage system for space. Cryogenics 2004;44:485–91.
[19] Wilson B, Mitchell R, Arritt B, Paul C, Hender D. The feasibility of cryogenic storage in space. In: International SAMPE technical conference, 2004. p. 613–24.
[20] Venkat S, Sherif SA. Self-pressurization and thermal stratification in a liquid hydrogen tank under varying gravity conditions. In: Proceedings of the 42nd AIAA aerospace sciences meeting and exhibit, 2004. p. 10844–54.
[21] Mukka SK, Rahman MM. Analysis of fluid flow and heat transfer in a liquid hydrogen storage vessel for space applications. In: Albuquerque, New Mexico Proceedings of the space technology and applications international forum (AIP); 2004.
[22] Mukka SK, Rahman MM. Computation of fluid circulation in a cryogenic storage vessel. In: Providence, Rhode Island Proceedings of the AIAA second international energy conversion engineering conference; 2004.
[23] Rahman MM, Ho SH. Zero boil-off cryogenic storage of hydrogen. In: Washington, DC Proceedings of the 2005 NHA hydrogen conference; 2005.
[24] Ho SH, Rahman MM. Three-dimensional analysis for liquid hydrogen in a cryogenic storage tank with heat pipe-pump system. Cryogenics 2007; in press, doi:10.1016/j.cryogenics.2007.09.005.
[25] Plachta DW, Christie RJ, Jurns JM, Kittel P. Passive ZBO storage of liquid hydrogen and liquid oxygen applied to space science mission concepts. Cryogenics 2006;46:89–97.
[26] White FM. Viscous fluid flow. 2nd ed. New York: McGraw Hill; 1991.
[27] Kays WM, Crawford ME, Weigand B. Convective heat and mass transfer. 4th ed. New York: McGraw Hill; 2005.
[28] Rodi W. Turbulence models and their application in hydraulics: state-of-the-art paper, 2nd revised ed. International Association for Hydraulic Research (IAHR); 1984.
[29] Fletcher CAJ. Computational Galerkin methods. New York: Springer; 1984.